Applied Surface Science 646 (2024) 158823

Contents lists available at ScienceDirect

Applied Surface Science

journal homepage: www.elsevier.com/locate/apsusc

Full Length Article

Platform for surface-enhanced Raman scattering in layered quantum materials

Hyun Jeong [a], Hyeong Chan Suh [a], Ga Hyun Cho [a], Rafael Salas-Montiel [b], Hayoung Ko [c], Ki Kang Kim [c,d], Mun Seok Jeong [a,*]

[a] Department of Physics, Hanyang University, Seoul 04763, Republic of Korea
[b] Laboratory Light, Nanomaterials and Nanotechnology - L2n CNRS EMR 7004, Université de Technologie de Troyes, 10004 Troyes, France
[c] Department of Energy Science, Sungkyunkwan University, Suwon 16419, Republic of Korea
[d] Center for Integrated Nanostructure Physics (CINAP), Institute for Basic Science (IBS), Sungkyunkwan University, Suwon 16419, Republic of Korea

ARTICLE INFO

Keywords:
Raman scattering
monolayer WSe_2
Gold micropillar
Surface plasmon
confocal Raman spectroscopy

ABSTRACT

Raman spectroscopy has been used to study transition metal dichalcogenides (TMDs), quantum materials with promising properties. However, monolayer (1L) TMDs have limited observable Raman modes due to low light absorption. In this study, we propose a potential platform that can effectively enhance Raman scattering and increase the number of observable Raman modes in 1L TMDs. To enhance Raman scattering in 1L TMDs, a platform was fabricated by forming large-scale periodic arrays of gold micropillars (MPs) using conventional photolithography followed by gold film deposition. 1L WSe_2 was transferred onto the Au MPs and Raman scattering was observed. The Raman intensity of 1L WSe_2 on Au MPs was 19 times higher than that of 1L WSe_2 on SiO_2 plates, and Raman modes difficult to detect in typical 1L WSe_2 are observed. Confocal Raman spectroscopic mapping revealed that the strong local Raman enhancement at the edge of the Au MP resulted in the amplification of Raman scattering in 1L WSe_2 on Au MP. This local field enhancement was theoretically verified using finite difference time domain (FDTD). The platform has industrial advantages and wide applicability due to its low cost, simple process, large controllable area, and short process time.

1. Introduction

Transition metal dichalcogenides (TMDs) are a class of layered quantum materials that have attracted significant attention for various applications such as electronics, optoelectronics, spintronics, sensors, and quantum computing owing to their unique structural, electronic, and optical properties [1–10]. In particular, when the TMD is a monolayer (1L), it displays direct bandgap properties, strong light–matter interaction, enhanced quantum effects, flexibility, and scalability [11–20]. As the applicability of TMDs increases, significant attention is being paid to Raman scattering. It can accurately and comprehensively observe and analyze the physical properties of TMDs [21–28]. Because Raman scattering is the inelastic scattering of photons by materials, multiple Raman modes are observed in multilayer or bulk TMDs [29–33]. However, in the case of 1L TMDs, the number of observable Raman modes and Raman intensities are significantly smaller than those for multilayer TMDs because of the low light absorption due to ultra-thin two-dimensional (2D) crystal lattice in 1L TMDs [34–36]. To overcome this limitation, Raman scattering enhancement of 1L TMDs by coupling with metal surface plasmons has recently been reported [37,38]. Yu *et al.* demonstrated Raman spectral enhancement in 1L MoS_2 by coupling plasmons with plasmonic nanogrooves [39]. Su *et al.* reported surface-enhanced Raman scattering of 1L TMDs on Ag nanorod arrays [40]. Using tip-enhanced Raman spectroscopy, Farhat *et al.* investigated the enhancement of Raman scattering in 1L MoS_2 by decorating it with gold nanoparticles [41]. However, the research results reported have been constrained by the requirement of expensive nanoscale processes, unavailability of controllable large-area fabrication, Raman scattering enhancement of less than 10 times, and non-observation of several Raman modes typically observed in multilayer TMDs.

In this paper, we propose an inexpensive, simple, and controllable large-scale substrate platform that can effectively enhance the Raman scattering of 1L TMDs. This platform enhanced the Raman scattering of 1L WSe_2, which is one of the most widely used TMDs, by approximately 20 times. Furthermore, the platform allows for the observation of Raman modes that are difficult to observe in a typical 1L WSe_2. The substrate platform was fabricated by creating periodic Au micropillars (MPs) by conventional photolithography, followed by deposition of an Au film. 1L

* Corresponding author.

https://doi.org/10.1016/j.apsusc.2023.158823
Received 17 September 2023; Received in revised form 24 October 2023; Accepted 31 October 2023
Available online 5 November 2023

WSe_2 was grown on an SiO_2 substrate using chemical vapor deposition (CVD). The surface morphology of periodic Au MP in a square array and 1L WSe_2 transferred to Au MP by wet transfer was verified by field emission scanning electron microscopy (FE-SEM). The thickness of the 1L WSe_2 and the diameter, height, and spacing of the Au MPs were verified by atomic force microscopy (AFM). Using Raman spectroscopy, the Raman spectrum of 1L WSe_2 was obtained for different substrate types. The number of observable Raman modes was compared and verified. Using confocal Raman spectroscopy mapping, we verified the specific region of 1L WSe_2 on the Au MPs that resulted in Raman scattering enhancement. Finally, the Raman scattering enhancement of 1L WSe_2 on Au MP was verified theoretically using finite-difference time-domain (FDTD).

2. Experimental

2.1. Synthesis of 1L WSe_2

Using a two-zone furnace CVD technique, the 1L WSe_2 was deposited on an SiO_2/Si substrate. In zone 1, the Se pellets were loaded to evaporate in the chamber. The cleaned SiO_2/Si substrate was then spin-coated with a tungsten precursor. The substrate coated with the W precursor was placed in the center of zone 2. Zone 1 was heated to 380 °C for Se evaporation. Meanwhile, zone 2 was heated to 780 °C, where the W precursor was placed. After 1L WSe_2 synthesis, the furnace was cooled rapidly to room temperature. All the growth processes proceeded under N2 and H2 atmospheres at flow rates of 500 and 6 sccm, respectively. All the growth process were proceeded under N_2 and H_2 atmosphere at flow rates of 500 and 6 sccm, respectively.

2.2. Fabrications for 1L WSe_2 on Au MPs

A SiO_2 substrate with a clean surface was prepared using conventional chemical cleaning. Maskless photolithography (LithoMaskless, Standard Science Inc.) was used to form the photoresist (P/R) MPs on the cleaned SiO_2 substrates. Radio frequency sputtering was used to deposit a 100 nm-thick Au film over the entire surface of the P/R MPs on the SiO_2 substrate to obtain the Au MPs. CVD-grown 1L WSe_2 was transferred to Au MPs using the PMMA-assisted wet transfer method.

2.3. Characterization

FE-SEM (S-4800, Hitachi) was performed to observe the surface morphology of the 1L WSe_2 on the Au MPs. Atomic force microscopy AFM (XE-100, Park system) was used to measure the topography of the Au MPs and 1L WSe_2 in the non-contact mode. Raman spectroscopy was performed using a commercial confocal Raman system (LabRam HR Evolution, HORIBA) equipped with a 532 nm laser, a 100 × objective (N. A. = 0.90), and an 1800-groove grating. The spatial resolution of the 2D Raman mapping images is approximately 300 nm. Photoluminescence spectroscopy was performed using the commercial equipment used to perform Raman spectroscopy. The excitation source was a 532 nm laser, and a 150-groove grating was applied.

2.4. FDTD simulation

Lumerical (ver. 2023R1, ANSYS) FDTD solutions were used for the FDTD simulations. A perfectly matched layer method was used for the boundary conditions. The local electric field in the edge region of the Au MP was first calculated. Then, the enhancement factor was evaluated as $EF = |E/E_0|^4$. The excitation wavelength was 532 nm. The incidence normal to the Au substrate was also considered.

3. Results and discussion

3.1. Integrated structure of 1L WSe_2 and large-scale periodic Au MP

Large-scale periodic Au MP arrays were fabricated using conventional photolithography and gold film deposition on SiO_2 substrates. The Au MPs were arranged in a square array with uniform size and spacing. The surface edges of the Au MPs were sharp because the Au film was deposited after the MPs were formed. (Fig. S1) The diameter and height of the Au MPs were 2 μm and 1 μm, respectively, and the distance between individual Au MPs were 2 μm (Fig. S2). CVD-grown 1L WSe_2 has a triangular shape and an average lateral size of 35 μm. Therefore, there are approximately 50 Au MPs under one flake. (Fig. S3) The thickness of the 1L WSe_2 was verified to be 0.7 nm by AFM topography. This value is consistent with the thickness of a typical 1L WSe_2, as reported previously (Fig. S4) [30,42–45]. CVD-grown 1L WSe_2 was transferred onto the Au MP array using the wet transfer method. During the transfer process, the 1L WSe_2 was subjected to a vertical downward force on the Au MPs. This resulted in a strong pulling force at the edge region of the Au MPs. This force caused the distance of 1L WSe_2 from the edge of the Au MP to be smaller than the van der Waals gap. Subsequently, this induced coupling of the surface plasmons localized at the edge of the Au MP. This, in turn, enhanced the Raman scattering of 1L WSe_2. Fig. 1a shows a three-dimensional (3D) illustration of the selectively enhanced Raman scattering of 1L WSe_2 on Au MPs. The Raman scattering of 1L WSe_2 could be enhanced at specific locations on the edge of the Au MP. Moreover, this enhanced Raman scattering enabled the observation of Raman modes that are challenging to observe in monolayers. Fig. 1b displays an SEM image of 1L WSe_2 transferred onto an Au MP array. The 1L WSe_2 transferred by wet transfer cover several Au MPs and is strongly attached to the edge region of the Au MPs. Because of this strong attachment, the distance between the 1L WSe_2 and the Au surface at the edge region of the Au MP can be shorter than the distance between the 1L WSe_2 and a flat surface. Fig. 1c presents a schematic illustration of the localized surface plasmon (LSP) on the Au MP and an approaching 1L WSe_2. The probability of surface plasmon coupling increases as the distance between the 1L WSe_2 and the surface of the Au MP decreases. This occurs because the intensity of the LSP electromagnetic field decreases exponentially with an increase in the distance from the Au surface. When the LSPs of the Au MPs interact with the 1L WSe_2 by reducing the distance between the 1L WSe_2 and Au MP, these induce a variation in the optical properties of the 1L WSe_2, including Raman scattering. An SEM image of the surface of the 1L WSe_2 on an individual Au MP is shown in Fig. 1d. The wrinkles in the 1L WSe_2 at the upper right corner of the image indicate that the 1L WSe_2 is being subjected to an outward pulling force applied by the Au MP.

3.2. Enhanced Raman scattering of 1L WSe_2 on Au MPs

In order to investigate the phonon modes of 1L WSe_2 on Au MPs, Raman spectroscopy was performed. The excitation source for Raman scattering was a continuous-wave (CW) laser with a wavelength of 532 nm. Fig. 2a shows the Raman spectra of the 1L WSe_2 according to the substrate type. A SiO_2 plate is commonly used as a substrate for growing 1L TMD because SiO_2 is inexpensive material and electrical insulator. It was employed as the reference substrate. In addition, an Au plate was used as a substrate to compare the effects of the structural features of the Au MPs. The red, blue, and black solid lines represent the Raman spectra of 1L WSe_2 on the Au MPs, Au plates, and SiO_2 plates, respectively. The Raman mode showing the strongest intensity is the peak of the combination of E' and A'_1 appearing at approximately 250 cm^{-1}. The next strongest Raman mode is the 2LA peak at approximately 260 cm^{-1} as indicated by the black arrows. As shown in Fig. 2a, the Raman intensity of 1L WSe_2 on the Au MPs is significantly higher than that of 1L WSe_2 on the SiO_2 plate as well as that on the Au plate. This indicates that the Raman scattering of 1L WSe_2 was enhanced by the interaction between

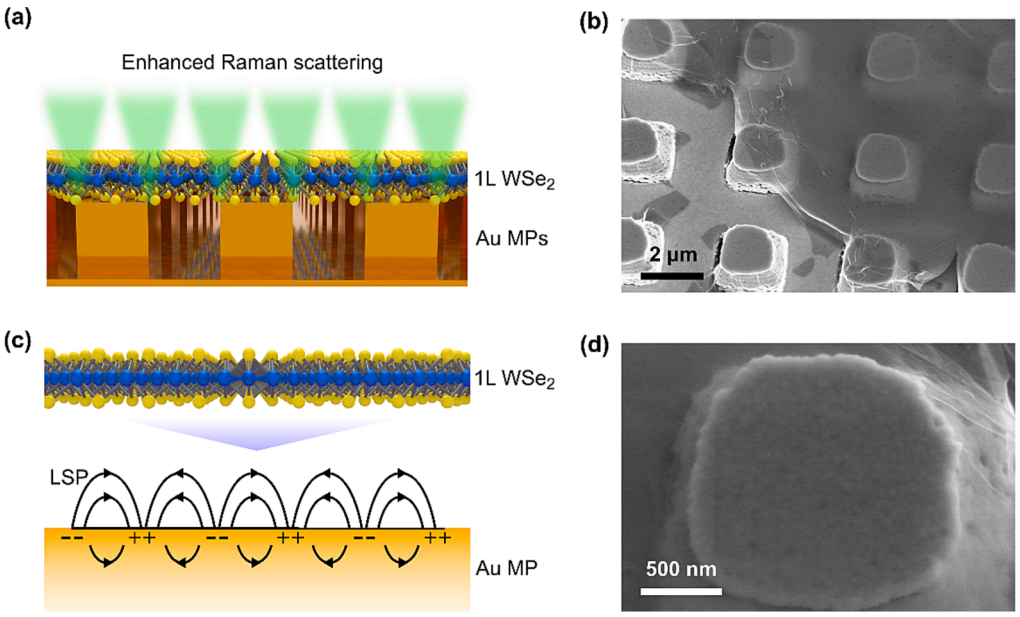

Fig. 1. 3D Schematics and SEM Images of 1L WSe_2 on Au MPs. (a) Three-dimensional (3D) illustration of the enhanced Raman scattering of 1L WSe_2 on Au MPs. The Raman scattering of 1L WSe_2 is enhanced at the edge region of Au MPs owing to LSP resonance. (b) SEM image of 1L WSe_2 transferred onto Au MPs by wet transfer method. The wet transfer method enables the transfer of 1L WSe_2 onto a large-area Au MP array. (c) 3D schematic of the interaction between 1L WSe_2 and an Au MP containing LSPs. As the 1L WSe_2 approaches the Au MP, the LSPs of the Au MP induce a transition in the optical properties of the 1L WSe_2, including Raman scattering. (d) SEM image of 1L WSe_2 on an individual Au MP. The 1L WSe_2 is subjected to an omnidirectional pulling force on the individual Au MPs. This minimizes the distance between the 1L WSe_2 and the Au MPs in the edge region of the Au MPs.

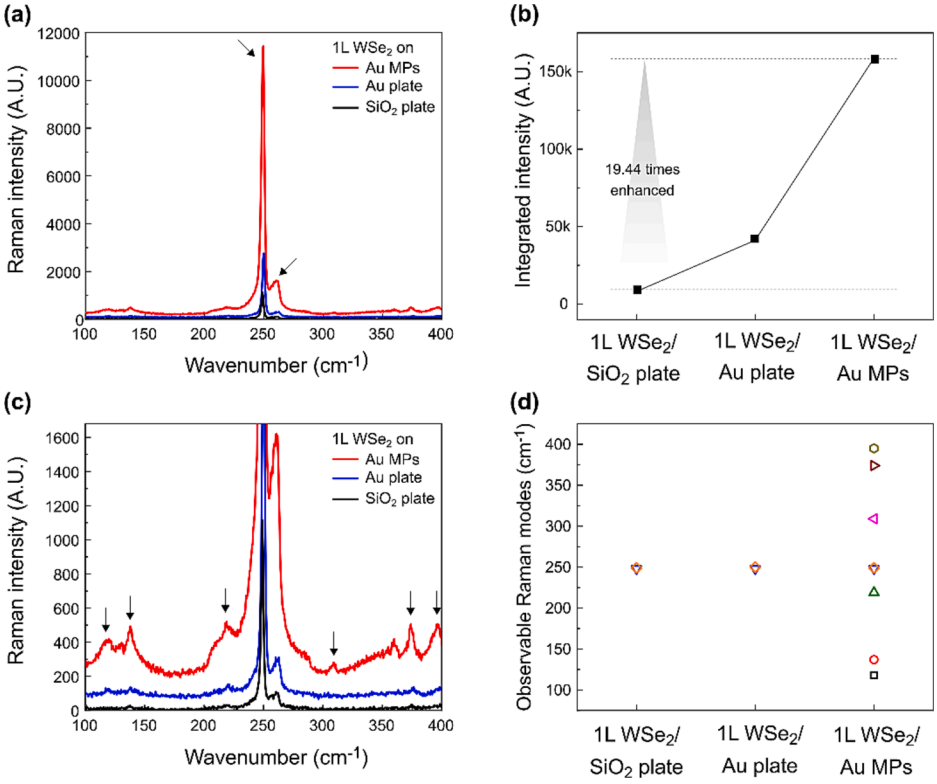

Fig. 2. Raman spectroscopy of 1L WSe_2 on different substrates. (a) Raman spectra of 1L WSe_2 on Au MPs, Au plate, and SiO_2 plate. The Raman intensity of 1L WSe_2 was enhanced significantly on the Au MPs compared with that on the Au and SiO_2 plates. (b) Raman spectra of 1L WSe_2 on different substrates with the y-axis magnified. Significantly more Raman modes are observed in the Raman spectrum of 1L WSe_2 on the Au MPs compared with that of 1L WSe_2 on the Au and SiO_2 plates. (c) Integrated intensity plot of the spectral region from 100 cm^{-1} to 400 cm^{-1} in the Raman spectrum of 1L WSe_2 on Au MPs, Au plate, and SiO_2 plate. The integrated intensity of 1L WSe_2 on the Au MPs is 19 times higher than that of 1L WSe_2 on the SiO_2 plate. (d) Plot of Raman modes observed in 1L WSe_2 on different substrates. Three Raman modes are observed for 1L WSe_2 on the SiO_2 and Au plates, whereas nine Raman modes are observed for 1L WSe_2 on the Au MPs.

1L WSe_2 and the Au MPs. To quantify the Raman scattering enhancement, the intensity of each spectrum was integrated in the range from 100 cm^{-1} to 400 cm^{-1}. Fig. 2b is a plot of the integrated intensity of each Raman spectrum. It is evident that the integrated intensity of 1L WSe_2 on the Au plate increased marginally compared with that on the SiO_2 plate. However, the integrated intensity of 1L WSe_2 on Au MPs increased substantially compared with the other two samples. In particular, the integrated intensity of 1L WSe_2 on the Au MPs increased by 19 times compared with that of 1L WSe_2 on the SiO_2 plate. This enhancement was significantly higher than that reported previously [46,47]. It can result in the appearance of peaks concealed by background noise as well as the enhancement of the main peaks. To verify the appearance of the concealed Raman modes, Fig. 2c shows the magnified Raman spectra. Several low-intensity peaks are observed in the Raman spectrum of 1L WSe_2 on Au MPs. These are not present in the Raman spectra of 1L WSe_2 on the Au plate and 1L WSe_2 on SiO_2 plate. The Raman modes observed only in the Raman spectrum of 1L WSe_2 on Au MPs are E'(M)^{LO2}-LA(M) at 118 cm^{-1}, A'$_1$(M)-LA(M) at 137 cm^{-1}, LA(M) + TA(M) at 219 cm^{-1}, B_{2g} at 309 cm^{-1}, E'(M)^{LO2}-LA(M) at 374 cm^{-1}, and 3LA(M) at 395 cm^{-1} [23,30,48,49]. These are indicated with black arrows. These Raman modes have generally been observed in multilayer WSe_2 or only in resonant Raman spectra in the case of a monolayer. However, in this study, the corresponding Raman modes were observed using typical Raman spectroscopy for monolayer WSe_2. In general, 1L TMDs have limited observable Raman modes because of their 2D features. However, the Au MPs template overcomes these limitations and enables the observation of concealed Raman modes in the 1L WSe_2. Fig. 2d shows a plot of the observable Raman modes for each sample. Three Raman modes are observed in the Raman spectra of 1L WSe_2 on the Au plate and 1L WSe_2 on the SiO_2 plate, whereas nine are observed in that of 1L WSe_2 on Au MPs. Table 1 lists the Raman modes and peak positions for each sample.

3.3. 2D Raman mapping of 1L WSe_2 on Au MP

Raman spectroscopy verified that the Raman scattering of 1L WSe_2 on Au MPs was enhanced. However, it was necessary to verify which region on the Au MPs was responsible for this enhancement. Therefore, the 2D Raman mapping of 1L WSe_2 on an individual Au MP was performed using confocal Raman spectroscopy. The excitation source for confocal Raman spectroscopy was a 532 nm CW laser. Fig. 3a shows the 2D Raman intensity mapping image of 1L WSe_2 on an individual Au MP. The brighter the color in the mapping image, the higher is the Raman intensity. The scale bar at the bottom left of the image indicates 1 μm. In the 2D Raman mapping image, the edge of the Au MP is indicated by a white dotted line. The Raman intensity of 1L WSe_2 is significantly higher along the edge region of the Au MP than in the other regions. The Raman intensity of 1L WSe_2 in the inside region of the Au MP is higher than that outside the Au MP. However, it is significantly lower than that in the edge region of the Au MP. To compare and analyze the Raman spectra of each region, the local Raman spectra of 1L WSe_2 measured at the edge, inside, and outside of the Au MP were extracted, as shown in Fig. 3b. The red, blue, and black solid lines represent the local Raman spectra of 1L WSe_2 at the edge, inside, and outside of the Au MP, respectively. The wavelength range of the Raman spectrum was set from 230 cm^{-1} to 270 cm^{-1}. These included two main peaks to compare the Raman intensity. Similar to the results of the 2D Raman mapping image, the intensity of the Raman spectrum of 1L WSe_2 is significantly higher in the edge region of the Au MP. These results imply that the enhanced Raman scattering in 1L WSe_2 on the Au MPs was impelled by the Raman enhancement of the 1L WSe_2 at the edge region of the Au MPs. To understand the relationship between the strongly enhanced Raman scattering of 1L WSe_2 in the edge region of the Au MP and the structural features of the sample, a 3D schematic of the cross-sectional structure of 1L WSe_2 on the Au MP (including the edge region of the Au MP) is shown in Fig. 3c. Based on the location of the Au MP, the region of 1L WSe_2 was divided into edges, inside, and outside. These are indicated with arrows. During the wet-transfer process, 1L WSe_2 was subjected to a pulling force from all the directions in the edge region of the Au MP. (Fig. S5) This force caused the distance between 1L WSe_2 and the Au surface to be shorter in the edge region than in the other areas. This is depicted in Fig. 3c. The reduced distance between 1L WSe_2 and the Au surface caused the coupling of the 1L WSe_2 to the surface plasmon of Au. This resulted in enhanced Raman scattering. The SEM image and 2D Raman mapping results also indicate that the distance between the 1L WSe_2 and the Au surface is the shortest in the edge region of the Au MP. To quantify and compare the Raman scattering enhancement, the integrated Raman intensity according to the measurement position of 1L WSe_2 on the Au MP is shown in Fig. 3d. The integrated intensities extracted from each representative area (edge, inside, and outside the Au MP) are displayed in red, blue, and black, respectively. Five Raman spectra were extracted from each representative region, and the minimum, maximum, and average values were plotted. Based on the average value, the integrated intensity of 1L WSe_2 in the edge area was 7.11 and 2.07 times higher than those outside and inside, respectively. The relatively higher-intensity fluctuation of 1L WSe_2 at the edge region of the Au MP is attributed to the non-uniform edge of the Au MP. It resulted in different Raman scattering enhancements. Nevertheless, the average value for 1L WSe_2 in the edge region of the Au MP was remarkably high compared with that in the other regions. This supports the assertion that the Raman scattering of 1L WSe_2 was enhanced by surface plasmon coupling in the edge region of the Au MP. In addition, the significantly enhanced photoluminescence (PL) intensity of 1L WSe_2 on Au MPs compared with that for Au plate and SiO_2 plate supports the coupling between the PL of 1L WSe_2 and the LSP of the Au MP at the edge of the Au MP [50,51]. (Fig. S6).

Table 1
Observable Raman modes with peak positions in 1L WSe_2 depending on the substrate.

Raman mode	1L WSe_2			Reference
	On SiO_2 plate (cm^{-1})	On Au plate (cm^{-1})	On Au MPs (cm^{-1})	
E'(M)^{LO2} -LA (M)	–	–	118	[48]
A'$_1$(M)-LA (M)	–	–	137	[23]
LA(M) + TA (M)	–	–	219	[30]
E'(Γ)	248	248	248	[48]
A'$_1$(Γ)	249	250	249	[48]
2LA(M)	261	262	261	[48]
B_{2g}	–	–	309	[49]
E'(M)^{LO2}-LA (M)	–	–	374	[48]
3LA(M)	–	–	395	[48]

3.4. Finite-difference time-domain (FDTD) for local field enhancement

To verify that the Raman scattering of 1L WSe_2 was enhanced in the edge region of the Au MP, the field enhancement was calculated using FDTD. The FDTD was performed using Lumerical, which is a commercial photonic simulation software package. A 1L WSe_2 was modeled as a 1 nm-thick flat layer on top of a step-edge Au-MP. The enhancement factor at a wavelength of 532 nm was calculated as

$$EF = \left|\frac{E}{E_0}\right|^4$$

E_0 is the initial amplitude of the input field, and E is the enhanced field at the 1L WSe_2 of the Au MP [52]. Fig. 4a–d shows the distribution of the local field enhancement when the distance between the 1L WSe_2 and Au MP is 0.5 nm, 1.0 nm, 3.0 nm, and 5.0 nm, respectively. The direction of

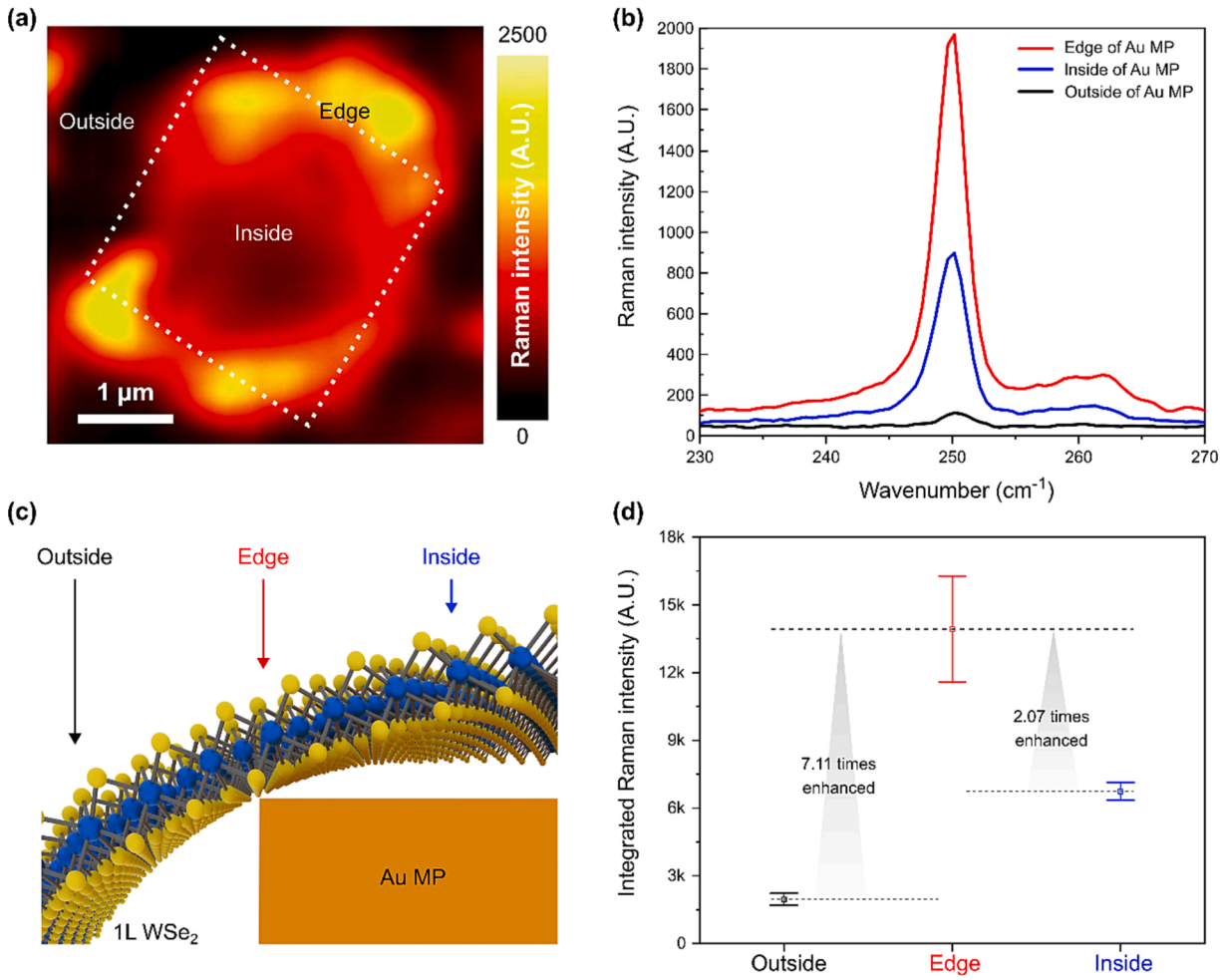

Fig. 3. Raman mapping of 1L WSe_2 on an individual Au MP. (a) Two-dimensional (2D) mapping image of the Raman intensity of 1L WSe_2 on an individual Au MP. The Raman intensity is highest at the edge region of the Au MP and lowest in the other regions. (b) Local Raman spectra extracted from 1L WSe_2 at the edge, interior, and exterior of the Au MP. The Raman intensity of 1L WSe_2 is highest at the edge of the Au MP and lowest outside the Au MP. (c) 3D schematic of 1L WSe_2 at the edge of the Au MP, showing the distance between 1L WSe_2 and the Au MP. The 1L WSe_2 is subjected to tensile forces in all the directions on the Au MP. This causes it to be stretched. The distance between the 1L WSe_2 and the Au surface is shortest at the edge of the Au MP, where the tensile forces are strongest. (d) Comparison of the integrated Raman intensities of 1L WSe_2 at different regions of the Au MP. The average integrated intensity of 1L WSe_2 at the edge of the Au MP is 7.11 times higher than that outside the Au MP.

propagation of the incident plane wave, E_0, was selected along the z-axis. Additionally, it was assumed that the electrical field was polarized along the × axis. As the 1L WSe_2 approached the Au MP, a strong field enhancement occurred because of the interaction between 1L WSe_2 and the Au surface. The variation in the enhancement factor with that in the gap between the 1L WSe_2 and the Au surface is plotted in Fig. 4e. The enhancement factor increased exponentially as the gap distance between 1L WSe_2 and the Au surface decreased. In particular, EF increased rapidly below 1 nm, where the gap distance was smaller than the van der Waals gap. This demonstrated the effect of the gap distance on the Raman enhancement of 1L WSe_2. The gap between the 1L WSe_2 and Au surface was reduced significantly in the edge region of the Au MP. It enabled the LSPs at the edge of the Au MP to be coupled to the 1L WSe_2. This significantly increased the field enhancement. As a result, the Raman scattering of 1L WSe_2 was enhanced substantially in the edge region of the Au MP, as shown in the inset of Fig. 4e. Therefore, FDTD theoretically supports the experimental results including Raman spectroscopy, 2D Raman mapping, SEM images, and Raman scattering enhancement of 1L WSe_2 by the surface plasmon coupling of Au MP.

4. Conclusions

In this study, an Au MP array with a low-cost, simple process and large-scale fabrication was introduced as a platform to effectively enhance the Raman scattering of 1L WSe_2. The SEM images show that multiple Au MPs were covered by 1L WSe_2 transferred using the wet transfer method. Raman spectroscopy was performed to verify the enhanced Raman scattering in 1L WSe_2 on the Au MPs. The Raman intensity of 1L WSe_2 on the Au MPs was enhanced by 19 times compared with that of 1L WSe_2 on the SiO_2 substrate. Moreover, nine Raman modes were observed in 1L WSe_2 on Au MPs, whereas only three Raman modes are observed in typical 1L WSe_2 owing to the 2D crystal lattice. Confocal Raman spectroscopy revealed that the Raman-scattering enhancement of 1L WSe_2 on the Au MPs occurred because of the locally enhanced Raman intensity in the edge region of the Au MPs. This was owing to the local field enhancement caused by the coupling between the LSPs of Au and 1L WSe_2 as the gap between 1L WSe_2 and the Au surface became exceptionally small in the edge region of the Au MP. According to the theoretical analysis of the FDTD results, a significant field enhancement occurred at the edge of the Au MP. The observations of this study would enable a more accurate and informative characterization of the optical, structural, and physical properties of layered

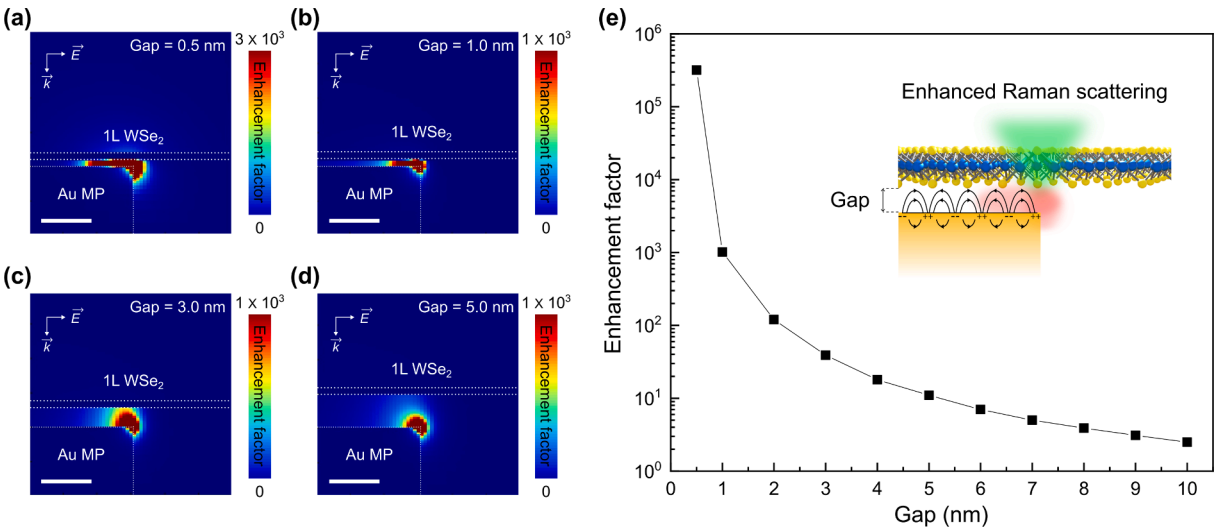

Fig. 4. Finite-difference time-domain (FDTD) of local field enhancement. FDTD simulations for local field enhancement between 1L WSe_2 and Au MPs with gap distance of (a) 0.5 nm, (b) 1.0 nm, (c) 3.0 nm, and (d) 5.0 nm. The simulations were performed in the edge region of the Au MP. The field enhancement factor was observed to be stronger when the distance between the 1L WSe_2 and Au MP was smaller. (e) Calculated enhancement factor as a function of the distance between 1L WSe_2 and the Au MP. The inset is a 3D schematic of the Raman enhancement mechanism. As the gap between 1L WSe_2 and the Au MP decreases, the Raman intensity is enhanced owing to the resonance of the phonons of 1L WSe_2 and LSPs of the Au MP.

quantum materials using Raman spectroscopy for applications in quantum technology.

Author contributions

The manuscript was written with contributions from all the authors. All the authors have approved the final version of the manuscript.

CRediT authorship contribution statement

Hyun Jeong: Conceptualization, Methodology, Investigation, Formal analysis, Data curation, Writing – original draft, Writing – review & editing. **Hyung Chan Suh:** Methodology, Data curation. **Ga Hyun Cho:** Methodology, Data curation. **Rafael Salas-Montiel:** Software, Validation. **Hayoung Ko:** Methodology. **Ki Kang Kim:** Resources. **Mun Seok Jeong:** Conceptualization, Funding acquisition, Resources, Project administration, Writing – review & editing, Supervision.

Declaration of Competing Interest

The authors declare that they have no known competing financial interests or personal relationships that could have appeared to influence the work reported in this paper.

Data availability

Data will be made available on request.

Acknowledgements

This research was supported by the Challengeable Future Defense Technology Research and Development Program through the Agency for Defense Development (ADD) funded by the Defense Acquisition Program Administration in 2022 (Grant No. UI220002TD), National Research Foundation of Korea (NRF) grant funded by the Korean government's Ministry of Science and ICT (MSIT)(No. 2022R1A2C2091945), and Basic Science Research Program through the National Research Foundation of Korea (NRF) funded by the Ministry of Education (NRF-2022R1I1A1A01073029). K.K.K. acknowledges support from the Basic Science Research Program and the Next-generation Intelligence Semiconductor Program through the National Research Foundation of Korea (NRF), funded by the Ministry of Science, ICT & Future Planning (2022R1A2C2091475, 2022M3F3A2A01072215). This study was supported by the Advanced Facility Center for Quantum Technology. The authors thank the French HPC Center ROMEO for partial support of computation resource.

Appendix A. Supplementary material

Supplementary data to this article can be found online at https://doi.org/10.1016/j.apsusc.2023.158823.

References

[1] X. Qian, J. Liu, L. Fu, J. Li, Quantum spin Hall effect in two-dimensional transition metal dichalcogenides, Science 346 (2014) 1344–1347, https://doi.org/10.1126/science.1256815.
[2] A. Kogar, M.S. Rak, S. Vig, A.A. Husain, F. Flicker, Y.I. Joe, L. Venema, G. J. MacDougall, T.C. Chiang, E. Fradkin, J. Van Wezel, P. Abbamonte, Signatures of exciton condensation in a transition metal dichalcogenide, Science 358 (2017) 1314–1317, https://doi.org/10.1126/science.aam6432.
[3] P. Rivera, H. Yu, K.L. Seyler, N.P. Wilson, W. Yao, X. Xu, Interlayer valley excitons in heterobilayers of transition metal dichalcogenides, Nat. Nanotechnol. 13 (2018) 1004–1015, https://doi.org/10.1038/s41565-018-0193-0.
[4] S.-Y. Xu, Q. Ma, Y. Gao, A. Kogar, A. Zong, A.M. Mier Valdivia, T.H. Dinh, S.-M. Huang, B. Singh, C.-H. Hsu, T.-R. Chang, J.P.C. Ruff, K. Watanabe, T. Taniguchi, H. Lin, G. Karapetrov, D. Xiao, P. Jarillo-Herrero, N. Gedik, Spontaneous gyrotropic electronic order in a transition-metal dichalcogenide, Nature 578 (2020) 545–549, https://doi.org/10.1038/s41586-020-2011-8.
[5] A. Ghiotto, E.-M. Shih, G.S.S.G. Pereira, D.A. Rhodes, B. Kim, J. Zang, A.J. Millis, K. Watanabe, T. Taniguchi, J.C. Hone, L. Wang, C.R. Dean, A.N. Pasupathy, Quantum criticality in twisted transition metal dichalcogenides, Nature 597 (2021) 345–349, https://doi.org/10.1038/s41586-021-03815-6.
[6] D.N. Basov, R.D. Averitt, D. Hsieh, Towards properties on demand in quantum materials, Nat. Mater. 16 (2017) 1077–1088, https://doi.org/10.1038/nmat5017.
[7] L. Wang, E.-M. Shih, A. Ghiotto, L. Xian, D.A. Rhodes, C. Tan, M. Claassen, D. M. Kennes, Y. Bai, B. Kim, K. Watanabe, T. Taniguchi, X. Zhu, J. Hone, A. Rubio, A. N. Pasupathy, C.R. Dean, Correlated electronic phases in twisted bilayer transition metal dichalcogenides, Nat. Mater. 19 (2020) 861–866, https://doi.org/10.1038/s41563-020-0708-6.
[8] T. Domröse, T. Danz, S.F. Schaible, K. Rossnagel, S.V. Yalunin, C. Ropers, Light-induced hexatic state in a layered quantum material, Nat. Mater. (2023), https://doi.org/10.1038/s41563-023-01600-6.
[9] C. Trovatello, A. Marini, X. Xu, C. Lee, F. Liu, N. Curreli, C. Manzoni, S. Dal Conte, K. Yao, A. Ciattoni, J. Hone, X. Zhu, P.J. Schuck, G. Cerullo, Optical parametric amplification by monolayer transition metal dichalcogenides, Nat. Photonics 15 (2021) 6–10, https://doi.org/10.1038/s41566-020-00728-0.
[10] Q. Li, A. Alfrey, J. Hu, N. Lydick, E. Paik, B. Liu, H. Sun, Y. Lu, R. Wang, S. Forrest, H. Deng, Macroscopic transition metal dichalcogenides monolayers with uniformly

high optical quality, Nat. Commun. 14 (2023) 1837, https://doi.org/10.1038/s41467-023-37500-1.
[11] M.M. Ugeda, A.J. Bradley, S.-F. Shi, F.H. Da Jornada, Y. Zhang, D.Y. Qiu, W. Ruan, S.-K. Mo, Z. Hussain, Z.-X. Shen, F. Wang, S.G. Louie, M.F. Crommie, Giant bandgap renormalization and excitonic effects in a monolayer transition metal dichalcogenide semiconductor, Nat. Mater. 13 (2014) 1091–1095, https://doi.org/10.1038/nmat4061.
[12] Y. Li, A. Chernikov, X. Zhang, A. Rigosi, H.M. Hill, A.M. Van Der Zande, D. A. Chenet, E.-M. Shih, J. Hone, T.F. Heinz, Measurement of the optical dielectric function of monolayer transition-metal dichalcogenides: MoS 2, Mo S e 2, WS 2, and WS e 2, Phys. Rev. B 90 (2014), 205422, https://doi.org/10.1103/PhysRevB.90.205422.
[13] M.-K. Lin, G.-H. Chen, C.-L. Ho, W.-C. Chueh, J.A. Hlevyack, C.-N. Kuo, T.-Y. Fu, J.-J. Lin, C.S. Lue, W.-H. Chang, N. Takagi, R. Arafune, T.-C. Chiang, C.-L. Lin, Tip-Mediated Bandgap Tuning for Monolayer Transition Metal Dichalcogenides, ACS Nano 16 (2022) 14918–14924, https://doi.org/10.1021/acsnano.2c05841.
[14] K. Falahati, A. Khatibi, B. Shokri, Light-matter interaction in tungsten Sulfide-based Janus monolayers: A First-Principles study, Appl. Surf. Sci. 599 (2022), 153967, https://doi.org/10.1016/j.apsusc.2022.153967.
[15] H. Zou, X. Wang, K. Zhou, Y. Li, Y. Fu, L. Zhang, Electronic property modulation in two-dimensional lateral superlattices of monolayer transition metal dichalcogenides, Nanoscale 14 (2022) 10439–10448, https://doi.org/10.1039/D2NR02189G.
[16] D.Y. Lee, C. Park, J. Choi, Y. Koo, M. Kang, M.S. Jeong, M.B. Raschke, K.-D. Park, Adaptive tip-enhanced nano-spectroscopy, Nat. Commun. 12 (2021) 3465, https://doi.org/10.1038/s41467-021-23818-1.
[17] Q. Zhang, Y. Zhang, G. Gao, S. Zhang, Potential-Driven Semiconductor-to-Metal Transition in Monolayer Transition Metal Dichalcogenides, Adv. Funct. Mater. 33 (2023) 2208736, https://doi.org/10.1002/adfm.202208736.
[18] D. Ding, Z. Qu, X. Han, C. Han, Q. Zhuang, X.-L. Yu, R. Niu, Z. Wang, Z. Li, Z. Gan, J. Wu, J. Lu, Multivalley Superconductivity in Monolayer Transition Metal Dichalcogenides, Nano Lett. 22 (2022) 7919–7926, https://doi.org/10.1021/acs.nanolett.2c02947.
[19] J.-D. Lin, P.-Y. Lo, G.-H. Peng, W.-H. Li, S.-Y. Huang, G.-Y. Chen, S.-J. Cheng, Essential role of momentum-forbidden dark excitons in the energy transfer responses of monolayer transition-metal dichalcogenides, Npj 2D Mater, Appl. 7 (2023) 51, https://doi.org/10.1038/s41699-023-00414-z.
[20] H. Jeong, H.M. Oh, A. Gokarna, H. Kim, S.J. Yun, G.H. Han, M.S. Jeong, Y.H. Lee, G. Lerondel, Integrated Freestanding Two-dimensional Transition Metal Dichalcogenides, Adv. Mater. 29 (2017) 1700308, https://doi.org/10.1002/adma.201700308.
[21] A.M. Dadgar, D. Scullion, K. Kang, D. Esposito, E.H. Yang, I.P. Herman, M. A. Pimenta, E.-J.-G. Santos, A.N. Pasupathy, Strain Engineering and Raman Spectroscopy of Monolayer Transition Metal Dichalcogenides, Chem. Mater. 30 (2018) 5148–5155, https://doi.org/10.1021/acs.chemmater.8b01672.
[22] X. Ma, P. Guo, C. Yi, Q. Yu, A. Zhang, J. Ji, Y. Tian, F. Jin, Y. Wang, K. Liu, T. Xia, Y. Shi, Q. Zhang, Raman scattering in the transition-metal dichalcogenides of 1 T′ − MoT e 2, T d − MoT e 2, and T d − WT e 2, Phys. Rev. B 94 (2016), 214105, https://doi.org/10.1103/PhysRevB.94.214105.
[23] X. Zhang, X.-F. Qiao, W. Shi, J.-B. Wu, D.-S. Jiang, P.-H. Tan, Phonon and Raman scattering of two-dimensional transition metal dichalcogenides from monolayer, multilayer to bulk material, Chem. Soc. Rev. 44 (2015) 2757–2785, https://doi.org/10.1039/C4CS00282B.
[24] X. Hou, Q. Lin, Y. Wei, Q. Hao, Z. Ni, T. Qiu, Surface-Enhanced Raman Scattering Monitoring of Oxidation States in Defect-Engineered Two-Dimensional Transition Metal Dichalcogenides, J. Phys. Chem. Lett. 11 (2020) 7981–7987, https://doi.org/10.1021/acs.jpclett.0c02318.
[25] J.-U. Lee, H. Cheong, Resonance Raman effects in transition metal dichalcogenides: Resonance Raman effects in transition metal dichalcogenides, J. Raman Spectrosc. 49 (2018) 66–75, https://doi.org/10.1002/jrs.5200.
[26] L.G. Pimenta Martins, B.R. Carvalho, C.A. Occhialini, N.P. Neme, J.-H. Park, Q. Song, P. Venezuela, M.S.C. Mazzoni, M.J.S. Matos, J. Kong, R. Comin, Electronic Band Tuning and Multivalley Raman Scattering in Monolayer Transition Metal Dichalcogenides at High Pressures, ACS Nano 16 (2022) 8064–8075, https://doi.org/10.1021/acsnano.2c01065.
[27] C. Liang, K. Sun, M. Chen, P. Xu, Crystal-Phase Engineering of Two-Dimensional Transition-Metal Dichalcogenides for Surface-Enhanced Raman Scattering: A Perspective, Langmuir 39 (2023) 11946–11953, https://doi.org/10.1021/acs.langmuir.3c01479.
[28] C. Lee, B.G. Jeong, S.J. Yun, Y.H. Lee, S.M. Lee, M.S. Jeong, Unveiling Defect-Related Raman Mode of Monolayer WS $_2$ via Tip-Enhanced Resonance Raman Scattering, ACS Nano 12 (2018) 9982–9990, https://doi.org/10.1021/acsnano.8b04265.
[29] R. Saito, Y. Tatsumi, S. Huang, X. Ling, M.S. Dresselhaus, Raman spectroscopy of transition metal dichalcogenides, J. Phys. Condens. Matter 28 (2016), 353002, https://doi.org/10.1088/0953-8984/28/35/353002.
[30] H. Terrones, E.D. Corro, S. Feng, J.M. Poumirol, D. Rhodes, D. Smirnov, N. R. Pradhan, Z. Lin, M.A.T. Nguyen, A.L. Elías, T.E. Mallouk, L. Balicas, M. A. Pimenta, M. Terrones, New First Order Raman-active Modes in Few Layered Transition Metal Dichalcogenides, Sci. Rep. 4 (2014) 4215, https://doi.org/10.1038/srep04215.
[31] H. Li, Q. Zhang, C.C.R. Yap, B.K. Tay, T.H.T. Edwin, A. Olivier, D. Baillargeat, From Bulk to Monolayer MoS2: Evolution of Raman Scattering, Adv. Funct. Mater. 22 (2012) 1385–1390, https://doi.org/10.1002/adfm.201102111.
[32] M. Grzeszczyk, K. Gołasa, M. Zinkiewicz, K. Nogajewski, M.R. Molas, M. Potemski, A. Wysmołek, A. Babiński, Raman scattering of few-layers MoTe $_2$, 2D Mater. 3 (2016), 025010, https://doi.org/10.1088/2053-1583/3/2/025010.
[33] E. Del Corro, H. Terrones, A. Elias, C. Fantini, S. Feng, M.A. Nguyen, T.E. Mallouk, M. Terrones, M.A. Pimenta, Excited Excitonic States in 1L, 2L, 3L, and Bulk WSe $_2$ Observed by Resonant Raman Spectroscopy, ACS Nano 8 (2014) 9629–9635, https://doi.org/10.1021/nn504088g.
[34] A.N. Barbosa, N.S. Figueroa, M. Giarola, G. Mariotto, F.L. Freire, Straightforward identification of monolayer WS2 structures by Raman spectroscopy, Mater. Chem. Phys. 243 (2020), 122599, https://doi.org/10.1016/j.matchemphys.2019.122599.
[35] H. Wu, M.-L. Lin, Y. Zhou, X. Zhang, P.-H. Tan, Analyzing Fundamental Properties of Two-Dimensional Materials by Raman Spectroscopy from Microscale to Nanoscale, Anal. Chem. 95 (2023) 10821–10838, https://doi.org/10.1021/acs.analchem.3c00272.
[36] A. Do Nascimento Barbosa, C.A.D. Mendoza, N.J.S. Figueroa, M. Terrones, F.L. Freire Júnior, Luminescence enhancement and Raman characterization of defects in WS2 monolayers treated with low-power N2 plasma, Appl. Surf. Sci. 535 (2021) 147685. 10.1016/j.apsusc.2020.147685.
[37] M. Rahaman, A.G. Milekhin, A. Mukherjee, E.E. Rodyakina, A.V. Latyshev, V. M. Dzhagan, D.R.T. Zahn, The role of a plasmonic substrate on the enhancement and spatial resolution of tip-enhanced Raman scattering, Faraday Discuss. 214 (2019) 309–323, https://doi.org/10.1039/C8FD00142A.
[38] A.I. Pérez-Jiménez, D. Lyu, Z. Lu, G. Liu, B. Ren, Surface-enhanced Raman spectroscopy: benefits, trade-offs and future developments, Chem. Sci. 11 (2020) 4563–4577, https://doi.org/10.1039/D0SC00809E.
[39] M.-W. Yu, S. Ishii, S. Li, C.-J. Ku, S.-Y. Chen, T. Nagao, K.-P. Chen, Enhancing Raman spectra by coupling plasmons and excitons for large area MoS2 monolayers, Appl. Surf. Sci. 605 (2022), 154767, https://doi.org/10.1016/j.apsusc.2022.154767.
[40] L. Su, L. Bradley, Y. Yu, Y. Yu, L. Cao, Y. Zhao, Y. Zhang, Surface-enhanced Raman scattering of monolayer transition metal dichalcogenides on Ag nanorod arrays, Opt. Lett. 44 (2019) 5493, https://doi.org/10.1364/OL.44.005493.
[41] P. Farhat, M.O. Avilés, S. Legge, Z. Wang, T.-K. Sham, F. Lagugné-Labarthet, Tip-Enhanced Raman Spectroscopy and Tip-Enhanced Photoluminescence of MoS $_2$ Flakes Decorated with Gold Nanoparticles, J. Phys. Chem. C 126 (2022) 7086–7095, https://doi.org/10.1021/acs.jpcc.1c10186.
[42] Y. Liu, Y. Huang, X. Duan, Van der Waals integration before and beyond two-dimensional materials, Nature 567 (2019) 323–333, https://doi.org/10.1038/s41586-019-1013-x.
[43] J. Huang, T.B. Hoang, M.H. Mikkelsen, Probing the origin of excitonic states in monolayer WSe2, Sci. Rep. 6 (2016) 22414, https://doi.org/10.1038/srep22414.
[44] S. Tongay, J. Suh, C. Ataca, W. Fan, A. Luce, J.S. Kang, J. Liu, C. Ko, R. Raghunathanan, J. Zhou, F. Ogletree, J. Li, J.C. Grossman, J. Wu, Defects activated photoluminescence in two-dimensional semiconductors: interplay between bound, charged and free excitons, Sci. Rep. 3 (2013) 2657, https://doi.org/10.1038/srep02657.
[45] G. Su, A. Gao, B. Peng, J. Hu, Y. Zhang, F. Liu, H. Zhang, P. Zhan, W. Wu, Observation of in-plane exciton–polaritons in monolayer WSe $_2$ driven by plasmonic nanofingers, Nanophotonics. 11 (2022) 3149–3157, https://doi.org/10.1515/nanoph-2022-0201.
[46] G. Yang, X. Fang, Y. Gu, A. Danner, F. Xie, X. Zhang, N. Lu, Y. Wang, B. Hua, X. Gu, Insights on the enhanced Raman scattering of monolayer TMDCs (Mo, W)(S, Se)2 with Ag nanoparticles via rapid thermal annealing, Appl. Surf. Sci. 520 (2020), 146367, https://doi.org/10.1016/j.apsusc.2020.146367.
[47] W. Yang, H. Li, J. Chen, J. Yin, J. Li, Y. Wu, B. Mo, T. Wu, B. Sun, Z. Wu, H. Wang, L. Dong, G. Wang, Plasmon-enhanced exciton emissions and Raman scattering of CVD-grown monolayer WS2 on Ag nanoprism arrays, Appl. Surf. Sci. 504 (2020), 144252, https://doi.org/10.1016/j.apsusc.2019.144252.
[48] W. Zhao, Z. Ghorannevis, K.K. Amara, J.R. Pang, M. Toh, X. Zhang, C. Kloc, P. H. Tan, G. Eda, Lattice dynamics in mono- and few-layer sheets of WS2 and WSe2, Nanoscale 5 (2013) 9677, https://doi.org/10.1039/c3nr03052k.
[49] P. Tonndorf, R. Schmidt, P. Böttger, X. Zhang, J. Börner, A. Liebig, M. Albrecht, C. Kloc, O. Gordan, D.R.T. Zahn, S. Michaelis De Vasconcellos, R. Bratschitsch, Photoluminescence emission and Raman response of monolayer MoS_2, MoSe_2, and WSe_2, Opt. Express 21 (2013) 4908, https://doi.org/10.1364/OE.21.004908.
[50] N.S. Mueller, R. Arul, G. Kang, A.P. Saunders, A.C. Johnson, A. Sánchez-Iglesias, S. Hu, L.A. Jakob, J. Bar-David, B. De Nijs, L.M. Liz-Marzán, F. Liu, J.J. Baumberg, Photoluminescence upconversion in monolayer WSe2 activated by plasmonic cavities through resonant excitation of dark excitons, Nat. Commun. 14 (2023) 5726, https://doi.org/10.1038/s41467-023-41401-8.
[51] A. Arora, T. Dixit, K.V. Anil Kumar, S. Krishnan, K. Lakshmi Ganapathi, A. Krishnan, P.K. Nayak, M.S. Ramachandra Rao, Plasmon induced brightening of dark exciton in monolayer WSe2 for quantum optoelectronics, Appl. Phys. Lett. 114 (2019), 201101, https://doi.org/10.1063/1.5093664.
[52] K. Kim, H.B. Lee, K.S. Shin, Surface-enhanced Raman scattering characteristics of nanogaps formed by a flat Ag substrate and spherical Pt nanoparticles, Spectrochim. Acta. A. Mol. Biomol. Spectrosc. 100 (2013) 10–14, https://doi.org/10.1016/j.saa.2012.01.049.